IEEE Access
Multidisciplinary ⋮ Rapid Review ⋮ Open Access Journal

Received 3 August 2024, accepted 16 August 2024, date of publication 27 August 2024, date of current version 6 September 2024.

Digital Object Identifier 10.1109/ACCESS.2024.3450707

RESEARCH ARTICLE

Ultra-Wideband Ultra-Thin Transmissive Linear to Circular Polarization Convertor Based on Crossed-Dipole-Shaped Metasurface

CHO HILARY SCOTT NKIMBENG[1], HEESU WANG[1], (Member, IEEE), DAEYEONG YOON[1,2], (Member, IEEE), YONG BAE PARK[1,2], (Senior Member, IEEE), HAEWOOK HAN[3], AND IKMO PARK[1], (Member, IEEE)

[1]Department of Electrical and Computer Engineering, Ajou University, Suwon 16499, Republic of Korea
[2]Department of AI Convergence Network, Ajou University, Suwon 16499, Republic of Korea
[3]Department of Electrical Engineering, Pohang University of Science and Technology, Pohang 37673, Republic of Korea

Corresponding authors: Ikmo Park (ipark@ajou.ac.kr) and Yong Bae Park (yong@ajou.ac.kr)

This work was supported in part by the National Research Foundation of Korea (NRF) grant funded by Korean Government Ministry of Science and ICT (MSIT) under Grant NRF-2022R1F1A1065324; in part by the Institute of Information and Communications Technology Planning and Evaluation (IITP) grant funded by Korean Government (MSIT), Development of 3D-NET Core Technology for High-Mobility Vehicular Service, under Grant 2022-0-00704-001; and in part by the Institute of Information and Communications Technology Planning and Evaluation (IITP) grant funded by Korean Government (MSIT) under Grant RS-2024-00396992.

ABSTRACT This paper presents an ultra-thin, ultra-wideband linear-to-circular (LTC) polarization converter based on the crossed-dipole-shaped metasurface. The unit cell of the crossed-dipole-shaped metasurface is made up of two identical T-shaped dipole arms, which are orthogonal to each other and are connected with a diagonal microstrip line. The LTC polarization converter is placed on the top side of an ultra-thin single-substrate layer with a profile size of 0.035 λ_o, where λ_o is a free space wavelength at the center frequency of the axial ratio bandwidth (20.89 GHz). The proposed design shows nearly equal transmission amplitude and stable phase difference of nearly 90° of the two orthogonal components of transmitted waves in a wide frequency range. The right-hand circularly polarized (RHCP) component of the transmitted wave is much larger than the left-hand circularly polarized, and thus, the transmitted wave is RHCP. Numerical and experimental results showed that the polarizer could realize an ultra-wideband LTC polarization conversion at both x- and y-polarized incidences in the frequency range from 11.66 to 30.12 GHz, which is a fractional bandwidth of 88.4%, and it can maintain a stable polarization conversion performance under large-range incidence angles. In addition, a high total transmittance of the electromagnetic wave was obtained.

INDEX TERMS Circular polarization, crossed-dipole, linear polarization, linear-to-circular polarization converter, transmission coefficient, ultra-wideband.

I. INTRODUCTION

The polarization state is an extremely important feature of electromagnetic wave propagation. The ability to manipulate the polarization state of electromagnetic waves can enable the control of electromagnetic waves for a wide range of applications [1], [2], [3]. Conventional methods of realizing polarization control include the utilization of the birefringence effect and optical activity of natural materials. These methods usually require a long propagation distance to obtain phase accumulation and have limitations on practical applications due to their bulky volume [4], [5]. In recent years, metasurfaces have provided a new way of polarization manipulation [6], [7], [8], [9], [10], [11], [12]. By controlling the amplitudes and phases of the reflected or transmitted waves, many metasurface polarization converters have been successfully investigated and demonstrated, such as transmissive [13], [14], [15], [16], [17], [18], [19], [20], [21], [22], [23], [24], [25], [26], [27], [28], [29] and reflective [30], [31], [32], [33], [34] linear-to-circular (LTC) polarization

The associate editor coordinating the review of this manuscript and approving it for publication was Bilal Khawaja.

conversion at linearly polarized (LP) incidence. LTC polarization converters in the transmissive mode are widely used due to their extensive applications in wireless communication systems [24]. In the design of transmissive LP-to-circularly polarized (CP) converters, the key factors taken into consideration are obtaining a wide axial ratio (AR) bandwidth, a high transmission coefficient, and a stable oblique incidence. Multilayer structures have been employed to achieve a broadband AR as well as a high transmission coefficient [13], [14], [15], [16], [17], [18]. However, these structures suffer bulky sizes and fabrication complexities. Single-layer polarization converters are a suitable candidate that can be used to solve the issue of bulky sizes and fabrication complexities and improve angular oblique incidence stability. However, the designs suffer from a narrow AR bandwidth [19], [20], [21], [22], [23], [24], [25]. Thus, the design of a single-layer LTC polarization converter with an ultra-wide AR bandwidth, which reduces both the profile size and fabrication complexity, is an important area of study.

A single-layer LTC polarization converter can be designed with a metallic layer on a single side of the substrate [24], [25] or with metallic layers on both sides of the substrate [19], [20], [21], [22], [23]. The significant advantage of using a single-layer LTC polarization converter with a double-sided metallic layer over a single-sided metallic layer is that it achieves good transmittance. However, to achieve a wide AR bandwidth with a double-sided metallic layer, the primary approach is to increase the profile size [19], [20]. A single-layered LTC polarization converter with a single-sided metallic layer has several advantages over the double-sided metallic layer configuration. There is a reduced fabrication complexity and cost with a single-sided metallic layer compared to the double-sided designs as it requires fewer fabrication steps and can be manufactured using conventional lithographic techniques. The additional advantage of single-sided metallic layer designs is the simplified integration with other components, such as lenses or filters, due to their simpler geometry. Furthermore, they exhibit improved angular oblique incidence stability compared to double-sided designs, as they are less sensitive to changes in the angle of incidence. These attributes make them more stable and suitable for practical applications. Thus, achieving a good transmittance with an ultra-wide AR bandwidth using a single-side metallic layer is an important area of research.

A single-layer LTC polarization converter with a double-sided metallic layer has been widely studied [19], [20], [21], [22], [23]. A wideband and wide-angle LTC polarization converter based on a single-layer dielectric substrate with a double-sided metallic layer was proposed [19]. The converter element was composed of a metal strip cross-backed by a strip horizontally and centrically located on the other metallic layer. This achieved wide bandwidth and stable performance at oblique incident angles, but suffered from a bulky profile and high insertion loss. The authors in [20] proposed a Jerusalem cross-like resonator and a metal strip placed back to back to achieve a wide AR bandwidth and stable oblique incidence. However, the structure's bulky profile size and high insertion loss remained drawbacks. In [21], a square ring with an enclosed diagonal split circular ring was used to design a dual-band LTC polarization converter. By using a thin substrate layer, a low profile, as well as low insertion losses, was realized. However, this structure only achieved narrow AR bandwidths in two frequency bands. Another design presented a wide-angle and wideband LTC polarization converter using a single dielectric substrate layer with a double-sided metallic layer [22]. This converter, featuring a large square aperture surrounding a concentric square-corner-truncated square patch, achieved stable performance at oblique incidence but exhibited a narrow bandwidth. For S-band CubeSat applications, a flexible LTC polarization converter with a double-sided metallic layer in a swastika-like shape was proposed in [23]. This design achieved an extremely narrow bandwidth with stable oblique incidence.

A few number of researchers have carried out research on the single-layer LTC polarization converter with a single-sided metallic layer [24], [25]. The authors in [24] proposed a design incorporates a hybrid meander line and loop configuration achieving a moderate bandwidth and stable performance at oblique incident angles. Another design utilized a split circular ring resonator enclosed in a square ring with three-stepped square patches [25]. The structure achieved narrow AR bandwidths at two distinct frequency bands with low insertion losses and demonstrated stable angular performance at different oblique angles for each band. The authors designed the dual-band structure due to its difficulties in achieving a stable phase difference of 90° and a good transmittance value over a wide frequency range. In our design, we addressed these challenges through careful optimization of the metasurface elements and the use of Rogers AD250C substrate, which offers excellent thermal and mechanical stability, minimizing performance variations, such as phase and transmittance over a broad frequency range.

In this paper, an ultra-thin single-layer single-sided metallic layer transmissive LTC polarization converter that exhibits an ultra-wide bandwidth is presented based on a novel crossed-dipole-shaped metasurface. It realizes ultra-wideband LTC polarization conversion at both the x- and y-polarized incidence. An ultra-wideband LTC polarization conversion, ranging from 11.66 to 30.12 GHz (fractional bandwidth of 88.4%) within which the AR is lower than 3 dB, is achieved. Additionally, an ultra-thin profile size of 0.035 λ_o, where λ_o is a free space wavelength at the center frequency of the AR bandwidth (20.89 GHz), is achieved a good transmittance of less than 2.4 dB within the AR bandwidth.

II. METASURFACE DESIGN AND OPERATION MECHANISM

Fig. 1 depicts the unit cell of the proposed LTC polarization converter metasurface, which comprises a single-layer Rogers AD250C substrate with dimensions of

3.5 mm × 3.5 mm × 0.508 mm (0.24 λ_o × 0.24 λ_o × 0.035 λ_o at 20.89 GHz) and a relative permittivity (ε_r) of 2.5 and a loss tangent ($tan\delta$) of 0.0015. The crossed-dipole-shaped unit cell consists of two identical crossed-dipole arms and is positioned on the top surface of the substrate only. Each crossed-dipole arm consists of two identical T-shaped dipoles that are orthogonal to each other and are connected with a diagonal microstrip line. The optimized geometrical parameters for the ultra-wideband ultra-thin LTC polarization converter are selected as $p = 3.5$ mm, $l_1 = 1.1$ mm, $l_2 = 1.575$ mm, $d_s = 0.412$ mm, $w_1 = 0.1$ mm, $w_2 = 0.15$ mm, $w_3 = 0.15$ mm $g_1 = 0.55$ mm, and $g_2 = 0.2$ mm.

Rogers AD250C was chosen as the substrate material due to its stable dielectric properties and low loss tangent, which help maintain performance across different environmental conditions. This material also exhibits excellent thermal stability and low moisture absorption, contributing to consistent performance even in varying environmental conditions. Additionally, its mechanical stability enhances the device's resilience against physical deformations. Additionally, Rogers AD250C was selected as the substrate material for its exceptional mechanical and thermal properties, which are crucial for maintaining the performance of the polarization converter in diverse environmental conditions. The substrate's high decomposition temperature (>500°C) and low moisture absorption (0.04%) ensure consistent performance under thermal stress and humid conditions. Furthermore, the mechanical stability of Rogers AD250C substrate ensures the device's resilience against physical deformation. These attributes collectively ensure that the polarization converter remains robust and reliable, even in challenging real-world conditions, including temperature fluctuations, humidity, and mechanical stress.

The design guidelines for the proposed unit cell are as follows:

- A crossed-dipole unit cell, which consists of two T-shaped dipole arms that are orthogonal to each other, is designed. The design of a conventional crossed-dipole is detailed in [35] and [36]. The T-shaped dipole arms serve as the core resonant elements crucial for achieving wideband operation. The resonant frequency of each dipole arm is fundamental to this design, facilitating a broader operational bandwidth by ensuring the resonances of these dipole arms overlap. Such overlapping of resonant frequencies is instrumental in extending the converter's bandwidth, enabling it to operate effectively over a wide range of frequencies.
- The widths of the dipole arms (w_1, w_2) are pivotal in defining the resonant characteristics and, consequently, the wideband performance of the converter. The arm widths influence the electromagnetic properties of the crossed-dipole unit cell, affecting both the capacitive and inductive reactions to incoming electromagnetic waves. These reactions are integral to tuning the unit cell's resonant frequency and achieving effective impedance matching across the desired frequency range.

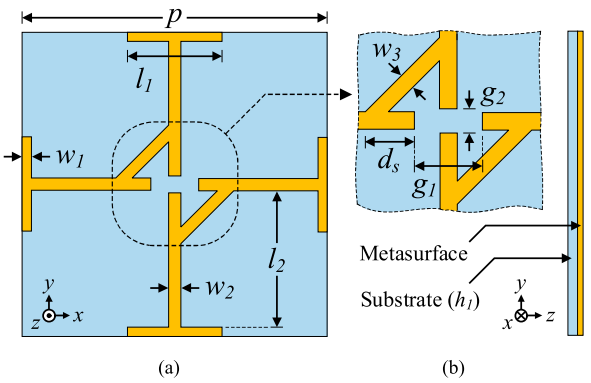

FIGURE 1. Unit cell for the proposed structure: (a) top view and (b) side view.

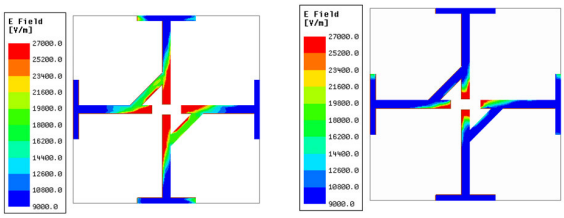

FIGURE 2. E-field distribution on dipole arms at 22.6 GHz: (a) 0°, 180° and (b) 90°, 270°.

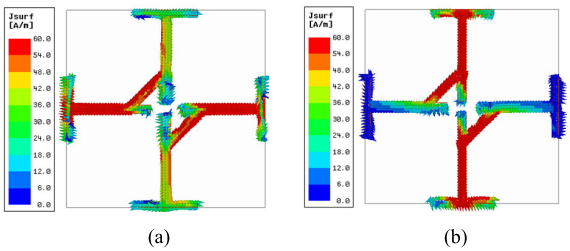

FIGURE 3. Surface current density (J_{surf}) on dipole arms at 22.6 GHz: (a) 0° and 180° and (b) 90° and 270°.

- To achieve a 90° phase difference, a diagonal microstrip line (w_3) is connected to the two T-shaped dipole arms. By fine-tuning the length and positioning of the microstrip line, the phase delay between the signals interacting with each arm can be accurately adjusted. Such precision ensures that the phase difference between the electromagnetic fields interacting with the dipole arms remains close to the desired 90° across an ultra-wide frequency band.
- The micro-split gaps, denoted as (g_1) and (g_2) are critical features in the crossed-dipole unit cell design that significantly influence the converter's capacitive properties. Located at the junctions where the T-shaped dipole arms meet, (g_1) and (g_2) introduce capacitance that is vital for fine-tuning the resonant frequency. The micro-split gaps, denoted as (g_1) and (g_2) are critical features in the crossed-dipole unit cell design that significantly influence the converter's capacitive properties. Located at the

junctions where the T-shaped dipole arms meet, (g_1) and (g_2) introduce capacitance that is vital for fine-tuning the resonant frequency. This fine-tuning is a key aspect of achieving a wide operational bandwidth because it enables the unit cell to resonate effectively over a larger range of frequencies.

- By fine-tuning these parameters, the converter achieves near-equal amplitudes and a consistent phase difference close to 90°, enabling reliable wideband operation.

The wideband operation of the crossed-dipole-shaped LTC polarization converter is achieved through a carefully engineered design that leverages the interaction of resonant elements, capacitive and inductive effects, and electromagnetic coupling. The T-shaped dipole arms, distinguished by their specific lengths (l_1, l_2) and widths (w_1, w_2), act as individual resonators each with distinct resonant frequencies. By designing these elements such that their resonant frequencies are closely aligned, a broader operational bandwidth is achieved. This broader bandwidth results from the overlapping resonances of these multiple elements, which combine to produce a broad, continuous frequency response.

Considering the LP plane wave from the z > 0 incident can be assumed on the surface of the xy-plane without insertion loss. The adopted LP wave of the 45° tilt incident can be decomposed into two even parts in horizontal and vertical directions, $\boldsymbol{E}_x^i$ and $\boldsymbol{E}_y^i$. Moreover, $\boldsymbol{E}_x^i$ and $\boldsymbol{E}_y^i$ should have the same magnitude and phase. Fig. 2 illustrates the high electric field intensities recorded on the vertical and horizontal gaps at 0° and 180°, as well as 90° and 270°, between the two T-shaped dipole arms in the crossed-dipole-shaped LTC polarization converter. These high field intensities create capacitance at the gaps, which is crucial for achieving the desired phase shift and amplitude distribution necessary for circular polarization. Therefore, we deduce that the capacitance results from the micro-split gaps g_1 and g_2 in the horizontal and vertical directions, respectively. The generation of capacitance through these gaps is crucial for the converter's ability to operate over a wide frequency range, as it enhances the device's capacitive and inductive characteristics, which are optimized to support wideband operation.

The dipole arm lengths (l_1, l_2) and widths (w_1, w_2), as well as the diagonal arm width (w_3), represent the overall inductance associated with the crossed-dipole-shaped LTC polarization converter in the x- and y-direction, respectively. The dipole arm length and width provide an inductive behavior for $\boldsymbol{E}_x^i$ and $\boldsymbol{E}_y^i$, as can be seen from the surface current distribution shown in Fig. 3. High current intensities are recorded for the horizontal dipole arm length and width for runs along the dipole arms at 0° and 180°, and high current intensities were noted in the vertical dipole arm at 90° and 270°. Varying the dipole arm lengths and widths in both the x- and y-direction leads to changes in the inductance. It thus provides different transmission characteristics to the two orthogonal electric field vectors, $\boldsymbol{E}_x^i$ and $\boldsymbol{E}_y^i$.This precision tuning of the inductance and capacitance allows the crossed-dipole-shaped LTC polarization converter to interact effectively with a broad spectrum of frequencies, optimizing its frequency response and supporting various resonant modes. Such adjustments directly contribute to minimizing signal loss and broadening the operational bandwidth, underpinning the converter's enhanced wideband functionality.

The diagonal microstrip arm of width (w_3) connected to the two T-shaped dipole arms helps to achieve a 90° phase difference between ϕ_x and ϕ_y. Varying the micro-split gaps (g_1) and (g_2), as well as the position of the diagonal microstrip arm, ensures that the phase of the y-direction part is advanced by ϕ_y, whereas that of the x-direction is delayed by ϕ_x, and thus, the phase difference $\Delta\phi = |\phi_y - \phi_x|$. Additionally, the interaction between the orthogonal dipole arms and the connecting diagonal microstrip arm is a critical aspect of the design, promoting multiple operational modes that enhance the bandwidth. The coupling between these elements ensures that various modes are excited at different frequencies, and their collective interaction leads to a comprehensive frequency response. Ideally, the transmitted wave can also be presented as the sum of two orthogonal LP components with equal magnitudes, $\boldsymbol{E}_x^t$ and $\boldsymbol{E}_y^t$ where $\boldsymbol{E}_x^t$ and $\boldsymbol{E}_y^t$ are transmitted electric field intensities of $\boldsymbol{E}_x^i$ and $\boldsymbol{E}_y^i$, respectively. Thus, by varying the capacitive and inductive parameters of the T-shaped dipole LTC polarization converter, the incident LP wave can be effectively converted to a CP wave.

III. EQUIVALENT CIRCUIT MODEL

The equivalent circuit model (ECM) of a crossed-dipole-shaped unit cell metasurface can be represented by a combination of lumped circuit elements, as well its corresponding impedance parameters are shown in Fig. 4 (a) and (b) respectively. In this model, E_1 and E_2 represent the electric field components in the two orthogonal directions of the crossed-dipole shaped LTC polarization converter, as shown in Fig. 5(a), and the circuit model for each orthogonal direction E_1 and E_2 are shown in Figs. 5(b) and (c), respectively.

The circuit consists of two lumped capacitors with C_1 and C_2, and two inductors with L_1 and L_2. The micro-split gaps g_1 and g_2 introduce capacitance (C_1 and C_2), indicating capacitive coupling between the dipole arms. Adjusting C_1 and C_2 fine-tunes this coupling, impacting the phase relationship and resonant behavior. When C_1 and C_2 are adjusted appropriately, the resonant frequencies of the dipole arms can be made to overlap or be very close to each other. This overlapping occurs because the tuning of C_1 and C_2 shifts the resonant points such that the frequency response of one dipole arm merges with or is adjacent to the frequency response of the other arm. The overlapping resonances create a continuous and broad frequency response. This overlapping is critical for wideband performance as it ensures that the polarization conversion remains effective across the entire desired frequency range, leading to a lower AR and stable CP conversion.

For effective linear-to-circular polarization conversion, maintaining a 90° phase difference between the orthogonal electric field components is crucial. Fine-tuning C_1 and C_2

helps achieve this across a wide frequency range by balancing capacitive effects. The resonant frequencies are determined by the interplay of inductance (L_1, L_2) and capacitance (C_1, C_2). Adjusting these values allows control over the resonant frequencies, enabling the dipole arms' responses to overlap, creating a broad frequency response and wide operational bandwidth, essential for a wide axial ratio (AR) bandwidth. The inductors L_1 and L_2 determined by the dipole arms' dimensions, (lengths l_1, l_2 and widths w_1, w_2 of the arms. Adjusting these dimensions shifts the resonant frequencies. For the dipole arms, the resonant frequencies in an LC circuit are given by

$$f_1 = \frac{1}{2\pi\sqrt{L_1 C_1}} f_2 = \frac{1}{2\pi}\sqrt{\frac{1}{L_2}\left(\frac{1}{C_1}+\frac{1}{C_2}\right)}$$

By varying L_1 and L_2, resonant frequencies f_1 and f_2 can be made to overlap, essential for wideband operation, ensuring the phase difference and transmission amplitude remain stable across a wide frequency range. This stability is vital for effective polarization conversion, maintaining the necessary 90° phase difference and equal transmission amplitude. Adjusting inductance through L_1 and L_2 enhances the unit cell's adaptability to different frequency bands, enabling wideband capabilities. Additionally, varying the inductors' values in both orthogonal directions ($\mathbf{E}_1$ and $\mathbf{E}_2$) modifies the T-shaped crossed-dipole unit cell's transmission characteristics, contributing to wideband performance. The transmission line accounts for the dielectric substrate's influence on the unit cell's performance. Considering the substrate material's properties, such as permittivity and thickness, helps accurately model the unit cell's behavior for wideband AR operation. When excited with an incident LP wave, the electric fields of the two dipoles combine to produce CP waves, achieved by maintaining a 90° phase difference and near-equal transmission amplitude. Adjusting the ECM's lumped elements converts the incident LP wave into a CP wave.

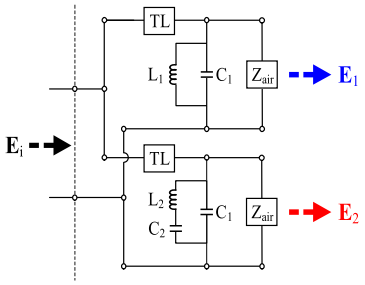

FIGURE 4. Equivalent circuit of T-shape crossed dipole unit cell.

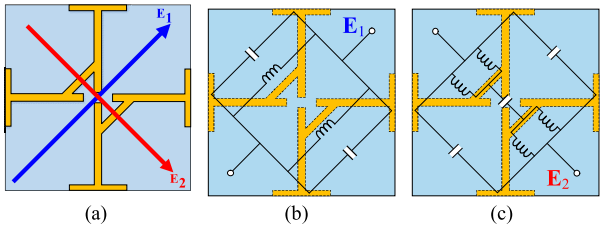

FIGURE 5. (a) Orthogonal vectors of unit cell, (b) equivalent circuit of orthogonal vector $\mathbf{E_1}$, and (c) Equivalent circuit of orthogonal vector $\mathbf{E_2}$.

IV. NUMERICAL ANALYSIS AND PARAMETRIC STUDY

To numerically investigate the LTC polarization conversion performance of the polarization converter design, we have carried out a series of numerical simulations by using Ansys High-Frequency Structure Simulator (HFSS) with the optimized geometrical parameters for the ultra-wideband LTC polarization converter given in Section II. Floquet ports, along with master-slave boundaries, were employed for the unit cell structure simulation. For the operation of the ultra-wideband unit cell, a plane electric field vector is oriented at $\varphi = 45^{o}$ to the x-axis relative to both the x- and y-axis. The incident electric field can be separated into two components with the same magnitude and phase in the x- and y-directions. If the y-polarized wave is incident along the +z direction, it transmits a cross-polarization component (y-to-x) of the incident electromagnetic wave, with magnitude and phase represented as t_{xy} and ϕ_{xy}, respectively. The co-polarization component (x-to-x) of the incident electromagnetic wave is also represented as t_{xx}. The LTC polarization converter is achieved when the two conditions of phase difference $\Delta\phi_{yx} = \arg(t_{xx})–\arg(t_{xy}) = \pm 90°$ and amplitude $|t_{xx}| = |t_{xy}|$ are satisfied. In general, when the AR of an electromagnetic wave is less than 3 dB, the electromagnetic wave can be regarded as a CP wave. To precisely determine the effective bandwidth of the proposed ultra-wideband LTC polarization converter, the AR of the transmitted wave was calculated based on the equation given in [20], [21], [22], [23], [24], [25], [26], [27], [28], [29], [30], [31], and [32]. The AR of the transmitted wave can be calculated as in Eq. (1):

$$\mathrm{AR} = \left(\frac{|t_{xx}|^2 + |t_{xy}|^2 + \sqrt{a}}{|t_{xx}|^2 + |t_{xy}|^2 - \sqrt{a}}\right)^{1/2} \tag{1}$$

where "a" can be computed from Eq. (2), as follows:

$$a = |t_{xx}|^2 + |t_{xy}|^2 + 2\,|t_{xx}|^2\,|t_{xy}|^2 \cos\left(2\Delta\phi_{xy}\right) \tag{2}$$

By substituting the values of the transmission coefficients t_{xx} and t_{xy}, as well as the phase difference $\Delta\phi_{yx}$ obtained from HFSS, into Eq. (1), the AR can be calculated. Fig. 6(a) illustrates the transmission coefficients of t_{xx} and t_{xy} showing that their magnitudes differ by less than 3 dB. Fig. 6(a) also shows that the phase difference $\Delta\phi_{yx}$ is close to 90^{o} within this frequency range. The achieved AR is lower than 3 dB over an ultra-wide frequency range, as shown in Fig. 6(b). This result confirms the successful realization of the anticipated LTC polarization conversion. The transmitted wave contains both RHCP and left-handed CP (LHCP) components, so we define Y-to-CP transmission coefficients as $t_{RHCP-y} = E^t_{RHCP}/E^i_y$ and $t_{LHCP-y} = E^t_{LHCP}/E^i_y$. This can be obtained using the

following formulas, respectively:

$$t_{RHCP-x} = \sqrt{2}\left(t_{xy} + jt_{xx}\right)/2 \quad (3)$$

$$t_{LHCP-x} = \sqrt{2}\left(t_{xy} - jt_{xx}\right)/2 \quad (4)$$

Based on the magnitude of the Y-to-CP transmission coefficient, we can deduce whether the transmitted wave is RHCP or LHCP. When the RHCP component in the transmitted wave is much larger than the LHCP, an RHCP transmitted wave is obtained. Also, when the LHCP component in the transmitted wave is much larger than the RHCP, an LHCP transmitted wave is obtained. Fig. 7(a) shows the magnitude of t_{RHCP-x} larger than the magnitude of t_{LHCP-x} over the ultra-wide frequency band. This implies that the transmitted wave is RHCP. Fig. 7(b) shows the total transmittance, which is computed using the formula $T_{all} = |t_{xx}|^2 + |t_{xy}|^2$. The insertion loss of the polarization converter can be kept lower than 2.3 dB within the AR bandwidth (12.13 to 30.19 GHz).

The response of the LTC polarization converter to changes in the incident angles is a vital aspect in the design of the ultra-wideband polarization converter. Sensitivity to changes in the angle of incidence could potentially limit performance in real-world applications where the angle of incidence varies. The polarization converter should be insensitive to changes in oblique incident angles. To investigate this, changes in the incident angles were applied, and the response variations in terms of the AR were analyzed. As shown in Fig. 8, the performance of the AR remained above 50% for incident angles less than $\pm 40^{o}$ for the simulated AR. However, as the incident angles continued to increase, the polarization conversion performance degraded rapidly.

Simulation and optimization of the ultra-wideband crossed-dipole unit cell metasurface were performed. The effects of key parameters of the unit cell characteristics were investigated. First, the response of the unit cell was determined when all parameters were fixed at their optimal values. Second, one design parameter was varied at a time during the parametric study. The effect of varying the crossed-dipole outer arm length (l_1) and crossed-dipole outer arm width (w_1) on the AR is shown in Figs. 9 and 10, respectively. As depicted on the left side of Fig. 9(a), as the crossed-dipole outer arm length (l_1) increases from 0.2 mm to 2.0 mm, the phase difference slightly deteriorates in the higher frequency. However, a good electromagnetic wave transmittance is maintained within the AR bandwidth, as the crossed-dipole outer-arm length (l_1) increases, as illustrated on the right-side of Fig. 9(a). Additionally, with an increase in the crossed-dipole outer arm length (l_1), the AR bandwidth slightly shifts to the lower frequencies and keeps deteriorating as the CP condition is not met due to large phase variations in the higher frequencies, as shown in Fig. 9(b). Similarly, as the crossed-dipole outer arm width (w_1) increases from 0.1 mm to 0.5 mm, the phase difference in the lower frequencies deteriorates while that of the higher frequency is closer to 90°. This leads to better CP performance in the higher frequency, and hence, a shift in the AR bandwidth to the higher

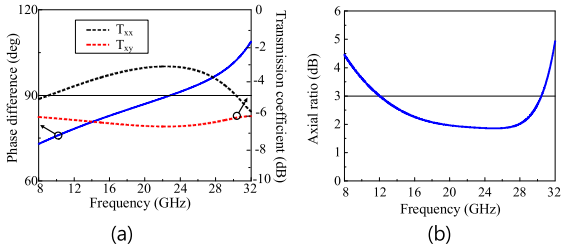

FIGURE 6. Responses of the unit cell: (a) phase and transmission coefficient, and (b) axial ratio.

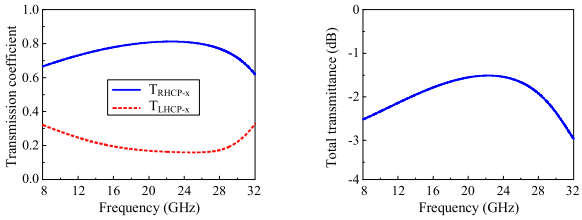

FIGURE 7. X-to-CP transmission coefficient of the proposed polarization converter at x polarized normal incidence and (b) total transmittance (T).

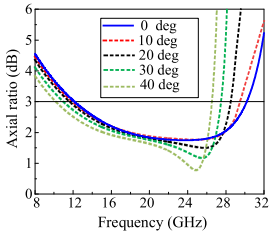

FIGURE 8. Simulated axial ratio variation with respect to the incident angle.

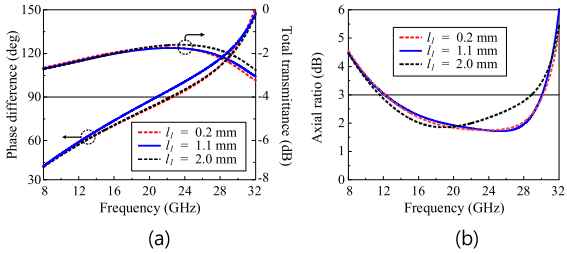

FIGURE 9. Effect of outer dipole arm length (l_1): (a) phase and transmittance, and (b) axial ratio.

frequencies, as shown on the left side of Fig. 10(a). Additionally, as shown on the right side of Fig. 10(a), an increase in the crossed-dipole outer arm width (w_1) from 0.1 mm to 0.5 mm leads to a deterioration in the transmittance at the lower frequencies. As shown in Fig. 10(b), when the crossed-dipole outer arm width (w_1) increases from 0.1 mm to 0.5 mm, the AR shifts to the higher frequencies because the phase in the lower frequencies is not close to 90° and the CP condition is not met in the lower frequencies. The effect of varying the crossed-dipole inner arm width (w_2) is depicted in Fig.11.

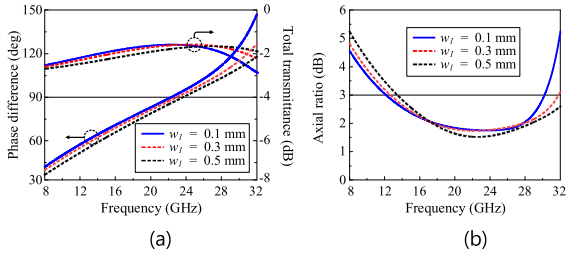

FIGURE 10. Effect of outer dipole arm width (w_1): (a) phase and transmittance, and (b) axial ratio.

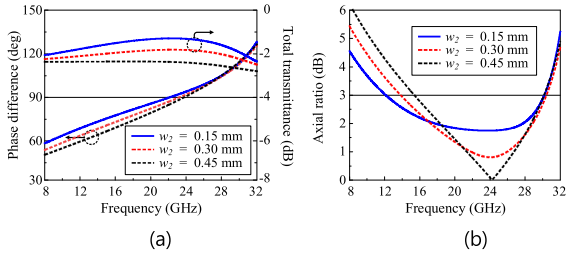

FIGURE 11. Effect of inner dipole width (w_2): (a) phase and transmittance, and (b) axial ratio.

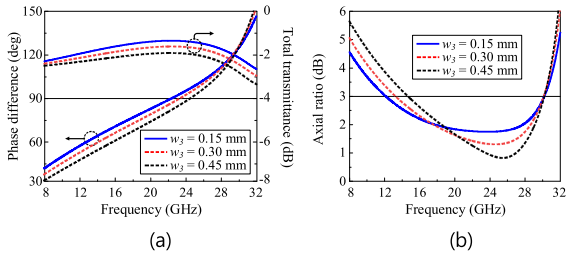

FIGURE 12. Effect of diagonal arm width (w_3): (a) phase and transmittance, and (b) axial ratio.

As the crossed-dipole inner arm width (w_2) increased from 0.15 to 0.45 mm, the phase difference in the lower frequencies deteriorated and did not meet the CP condition, whereas the phase difference at higher frequencies approached 90°, as displayed on the left side of Fig. 11(a). Additionally, it was evident that an increase in the crossed-dipole inner arm width (w_2) from 0.15 to 0.45 mm resulted in rapid degradation of the electromagnetic wave transmittance, as depicted on the right side of Fig. 11(a). Therefore, the crossed-dipole inner arm width (w_2) can be considered a crucial parameter for controlling electromagnetic wave transmittance. As demonstrated in Fig. 11(b), an increase in the crossed-dipole inner arm width (w_2) resulted in an upward shift of the AR bandwidth. The effect of varying the width of the diagonal arm (w_3) on the AR bandwidth is depicted in Fig. 12. As the width of the diagonal arm decreased from 0.45 to 0.15 mm, the phase difference improved significantly, as demonstrated on the left side of Fig. 12(a). Additionally, the total transmittance of the electromagnetic wave also improved significantly as the width of the diagonal arm (w_3) decreased, as displayed on the right side of Fig. 12(a). Furthermore, as the width of the diagonal arm (w_3) decreased, the AR shifted to the lower frequencies, as depicted in Fig. 12(b). The crossed-dipole inner arm length (l_2) can be varied by changing the gap size (g_1), as shown in Fig. 11. Increasing the gap size (g_1) from 0.55 to 1.35 mm resulted in a decrease in the crossed-dipole inner arm length (l_2). As the gap size (g_1) increased, the phase difference at higher frequencies improved and approached 90°, as demonstrated on the left side of Fig. 13(a). Moreover, as the gap size (g_1) increased, the total electromagnetic wave transmittance improved at higher frequencies, as displayed on the right side of Fig. 13(a). As demonstrated in Fig. 14(b), an increase in the gap size (g_1) resulted in an upward shift in the AR bandwidth. Additionally, the crossed-dipole inner arm length (l_2) could also be affected by varying the gap size (g_2). Increasing the gap size (g_2) from 0.2 to 0.6 mm resulted in a decrease in the crossed-dipole inner arm length (l_2). As demonstrated on the left side of Fig. 14(a), as the gap size (g_2) increased, the phase difference at higher frequencies improved and moved closer to 90°. Additionally, an increase in the gap size (g_2) resulted in enhanced electromagnetic wave transmittance, as displayed on the right side of Fig. 14(b). As demonstrated in Fig. 14(b), an increase in the gap size (g_2) also resulted in a shift in the AR bandwidth at higher frequencies. This result implied that the AR bandwidth could be improved by increasing the gap sizes g_1 and g_2.

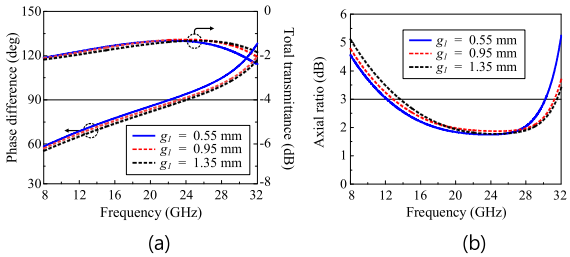

FIGURE 13. Effect of gap size (g_1): (a) phase and transmittance, and (b) axial ratio.

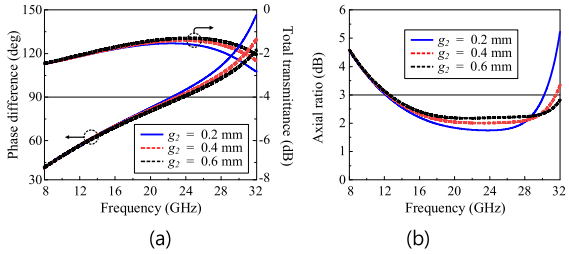

FIGURE 14. Effect of gap size (g_2): (a) phase and transmittance, and (b) axial ratio.

V. MEASUREMENT RESULTS

To demonstrate the performance of the proposed ultra-thin and ultra-wideband LTC polarization conversion structure, a sample was fabricated using the standard printed circuit board technique, which contained 50 × 50 cells and occupied an area of 175 mm × 175 mm. The fabricated prototype is presented in Fig. 15(a), while the measurement setup is

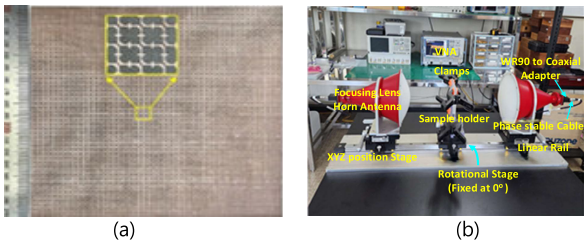

(a) (b)

FIGURE 15. (a) Fabricated sample and (b) experimental setup.

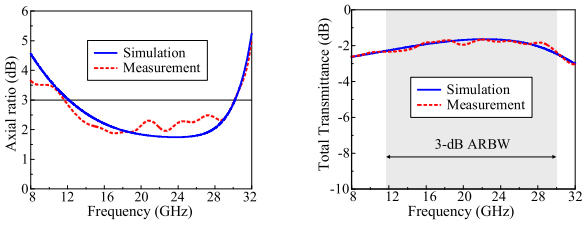

(b) (b)

FIGURE 16. Simulation and measurement results: (a) axial ratio and (b) transmittance.

displayed in Fig. 15(b). The horn antenna was mounted on a rail, providing the flexibility to adjust the distance between the sample and the antenna. To achieve precise movements, an xyz-position stage was installed, ensuring that the sample holder maintained the same distance from the horn antenna as the focal length.

Additionally, the sample holder was equipped with a rotating stage, enabling adjustment of the angle of incidence for electromagnetic waves interacting with the sample. It is important to note that since the direction of the antenna was fixed, altering the angle of incidence allowed for exclusive measurements of the transmittance. To minimize the impact of reflection and diffraction, a focusing lens horn antenna was selected. As a result, the diffraction effect arising from the clamp became negligible and could be disregarded. For the connection between the horn antenna and the vector network analyzer (VNA), a waveguide to coaxial adapter, flange, and cables were employed, ensuring a reliable and accurate connection. As presented in Fig. 15(b), two horn antennas were connected to an Agilent VNA (N5230C), between which the sample was positioned. During the measurements, one horn antenna was used to emit the vertically polarized (x-polarized) incident waves, while the other was employed to receive the vertically polarized transmission waves to obtain the transmission coefficient (t_{xx}). Then, we fixed the two horns and rotated the sample by 90° to test the transmission coefficient (t_{xy}).

As demonstrated in Fig. 16, there was good agreement between the measured and simulated results. In Fig. 16(a), it is evident that the measured 3 dB AR bandwidth was approximately equal to 88.4%, ranging from 11.66 to 30.12 GHz, while the simulated 3 dB AR bandwidth was approximately equal to 85.35% from 12.13 to 30.19 GHz. Additionally, Fig. 16(b) demonstrates that the measured

TABLE 1. Performance comparison of the proposed LTC polarization converter with other single-layer LTC polarization converters.

Ref. No.	T (λ_o)	CS (λ_o)	IL (dB)	BW (%)	AS (°)	ML	CF (GHz)
[19]	0.13	0.11 × 0.21	3	70	55	2	24.15
[20]	0.11	0.29 × 0.29	1.9	69	30	2	9.35
[21]	0.017	0.30 × 0.3	1.6	25	-	2	17.8,
	0.036	0.63 × 0.6	2.8	16.4			36.5
[22]	0.075	0.25 × 0.25	2.19	37.3	45	2	9.38
[23]	0.02	0.42 × 0.48	–	5.39	30	2	2.45
[24]	0.02	0.15 × 0.27	3	46.8	30	1	23.5
[25]	0.005	0.24 × 0.24	2.3	41	45	1	13.9
	0.16	0.48 × 0.48	2	23	30		28.5
This work	0.035	0.24 × 0.24	2.4	88.4	40	1	20.89

T: thickness, CS: cell size, IL: insertion loss, BW: 3 dB AR bandwidth, AS: angular stability, ML: metallic layer, CF: center frequency.

transmittance within the AR bandwidth ranged from −2.37 to −1.64 dB, while the simulated transmittance within the AR bandwidth ranged from −2.29 to −1.57 dB. This difference between the simulations and experimental results was probably caused by fabrication and measurement tolerances.

VI. COMPARISON

Table 1 presents a comparison of the proposed ultra-wideband and other single-layered LTC polarization converters. The comparison indicates that the proposed converter achieved an excellent overall performance, including a broadband AR bandwidth and an ultrathin profile size, compared to the other polarization converters [19], [20], [21], [22], [23], [24], [25]. The proposed structure also exhibited better transmittance compared to the work in [19] and [24], although the transmittance of the work in [20], [21], and [22] was slightly better compared to that of our proposed structure. The design by Wang et al. [19] exhibited superior angular stability (55°) compared to the proposed design. However, the proposed structure had better transmittance (0.7 dB), a lower profile size, and a wider AR bandwidth. Gao et al.'s [20] design had a total transmittance of less than 1.9 dB, which was 0.5 dB better than the proposed structure. However, it had a larger profile size and a narrower AR bandwidth (69%) compared to the proposed structure (85.5%). Additionally, the proposed structure demonstrated superior angular stability. The design by Fahad et al. [21] had a total transmittance in the lower frequency band that was 0.8 dB better than that of the proposed structure. However, in the higher frequency band, the proposed structure achieved a better transmittance of 0.4 dB and AR bandwidths of 25% and 16.4%, respectively, and the two distinct frequency bands were narrower than that of

the proposed structure. In Lin et al.'s [22] study, the total transmittance of their design was 0.21 dB better than the proposed structure and also exhibited a better angular stability of 45° compared to the proposed structure's 40°. However, it had a larger profile size and a narrower AR bandwidth (37.3%). In the work by Mirza et al. [23], total transmittance was not mentioned. However, they achieved a lower profile structure (0.02λ) compared to the proposed structure but had the drawbacks of narrow AR bandwidth (5.39%) and lower angular stability (30°). Fei et al. [24] achieved a lower profile size (0.02λ) compared to the proposed structure, but the transmittance was 0.7 dB lower. Additionally, the AR bandwidth (46.8%) was narrower than the proposed structure, and the proposed structure also had superior angular stability. The total transmittance of the design in [25] was similar to that of the proposed structure in the lower frequency band and 0.4 dB better in the higher frequency band. However, the AR bandwidths in both frequency bands (41% and 23%, respectively) were narrower than those of the proposed structure. The angular stability was better in the lower band (45°) compared to the proposed structure, but lower in the higher frequency band (30°). In conclusion, the proposed ultra-wideband LTC polarization converter demonstrates superior overall performance compared to the other single-layered LTC polarization converters [19], [20], [21], [22], [23], [24], [25]. It achieves a broader AR bandwidth and excellent transmittance. Although some designs exhibit slightly better transmittance or lower profile sizes, they generally suffer from narrower AR bandwidths or compromised angular stability. The proposed structure offers an optimal balance of AR bandwidth, profile size, transmittance, and angular stability, making it an excellent choice among the evaluated designs.

VII. CONCLUSION

This paper presented an ultra-thin, ultra-wideband, LTC polarization converter based on a crossed-dipole-shaped metasurface. The polarization converter comprises two identical crossed-dipole arms, with each crossed-dipole arm consisting of two identical T-shaped dipole arms that are orthogonal to each other and are connected with a diagonal microstrip line. By adjusting the design parameters of the converter, a stable phase difference of close to 90° with a near-equal amplitude of the transmitted waves was achieved over an ultra-wide frequency band. Thus, LP to CP conversion was obtained in the ultra-wide frequency band. The results indicated that a 3 dB AR bandwidth of the polarizer was achieved in a frequency range of 11.66 to 30.12 GHz (88.4%) at a normal incidence. The anticipated LP-to-CP polarization conversion could be realized in this frequency band at both x- and y-polarized incidences with an ultrathin profile size of $0.035\ \lambda_o$. Additionally, a high transmittance of electromagnetic waves was obtained with a single layer. The proposed structure has an ultrathin thickness and ultra-wide bandwidth compared to the reported designs, facilitating its use in many applications, such as antennas and remote sensors.

REFERENCES

[1] M. Barozzi and A. Vannucci, "Dynamics of lossless polarization attraction," *Photon. Res.*, vol. 3, no. 5, pp. 229–233, 2015.

[2] J. Zhang, J. Yang, H. Lu, W. Wu, J. Huang, and S. Chang, "Polarization-independent grating coupler based on silicon-on-insulator," *Chin. Opt. Lett.*, vol. 13, no. 9, 2015, Art. no. 091301.

[3] Q. Wu, F. Lan, Y. X. Zhang, H. X. Zeng, Z. Yang, and X. Gao, "Polarization insensitivity in square split-ring resonators with asymmetrical arm widths," *Chin. Opt. Lett.*, vol. 13, no. 10, 2015, Art. no. 101601.

[4] Y. Zhao and A. Alù, "Manipulating light polarization with ultrathin plasmonic metasurfaces," *Phys. Rev. B, Condens. Matter*, vol. 84, no. 20, Nov. 2011, Art. no. 205428.

[5] H.-Y. Chen, J.-F. Wang, H. Ma, S.-B. Qu, J.-Q. Zhang, Z. Xu, and A.-X. Zhang, "Broadband perfect polarization conversion metasurfaces," *Chin. Phys. B*, vol. 24, no. 1, Jan. 2015, Art. no. 014201.

[6] I. Park, "Application of metasurfaces in the design of performance-enhanced low-profile antennas," *EPJ Appl. Metamater.*, vol. 5, no. 11, pp. 1–12, 2018.

[7] C. H. S. Nkimbeng, H. Wang, and I. Park, "Coplanar waveguide-fed bidirectional same-sense circularly polarized metasurface-based antenna," *J. Electromagn. Eng. Sci.*, vol. 21, no. 3, pp. 210–217, Jul. 2021.

[8] B. Rana, I.-G. Lee, and I.-P. Hong, "Experimental characterization of 2×2 electronically reconfigurable 1 bit unit cells for a beamforming transmitarray at X band," *J. Electromagn. Eng. Sci.*, vol. 21, no. 2, pp. 153–160, Apr. 2021.

[9] C. H. S. Nkimbeng, H. Wang, and I. Park, "Low-profile wideband unidirectional circularly polarized metasurface-based bowtie slot antenna," *IEEE Access*, vol. 9, pp. 134743–134752, 2021.

[10] C. H. S. Nkimbeng, H. Wang, G. Byun, Y. B. Park, and I. Park, "Non-uniform metasurface integrated circularly polarized end-fire dipole array antenna," *J. Electromagn. Eng. Sci.*, vol. 23, pp. 29–41, 2023.

[11] C. H. S. Nkimbeng and I. Park, "Series-fed printed dipole array incorporated with linear to circular polarization metasurface converter," in *Proc. 14th Global Symp. Millim.-Waves THz (GSMM)*, May 2022, pp. 69–71.

[12] S. X. Ta and I. Park, "Compact wideband circularly polarized patch antenna array using metasurface," *IEEE Antennas Wireless Propag. Lett.*, vol. 16, pp. 1932–1936, 2017.

[13] W. Zhang, J.-Y. Li, and J. Xie, "A broadband circular polarizer based on cross-shaped composite frequency selective surfaces," *IEEE Trans. Antennas Propag.*, vol. 65, no. 10, pp. 5623–5627, Oct. 2017.

[14] L. Martinez-Lopez, J. Rodriguez-Cuevas, J. I. Martinez-Lopez, and A. E. Martynyuk, "A multilayer circular polarizer based on bisected split-ring frequency selective surfaces," *IEEE Antennas Wireless Propag. Lett.*, vol. 13, pp. 153–156, 2014.

[15] S. M. A. Momeni Hasan Abadi and N. Behdad, "Wideband linear-to-circular polarization converters based on miniaturized-element frequency selective surfaces," *IEEE Trans. Antennas Propag.*, vol. 64, no. 2, pp. 525–534, Feb. 2016.

[16] B.-Q. Lin, J.-X. Guo, B.-G. Huang, L.-B. Fang, P. Chu, and X.-W. Liu, "Wideband linear-to-circular polarization conversion realized by a transmissive anisotropic metasurface," *Chin. Phys. B*, vol. 27, no. 5, May 2018, Art. no. 054204.

[17] W. Zhang, J.-Y. Li, and J. Xie, "A broadband linear-to-circular transmission polarizer based on right-angled frequency selective surfaces," *Int. J. Antennas Propag.*, vol. 2017, no. 1, 2017, Art. no. 8067574.

[18] Z. Guo, X. Cao, J. Gao, H. Yang, and L. Jidi, "A novel composite transmission metasurface with dual functions and its application in microstrip antenna," *J. Appl. Phys.*, vol. 127, no. 11, Mar. 2020, Art. no. 115103.

[19] H. B. Wang, Y. J. Cheng, and Z. N. Chen, "Wideband and wide-angle single-layered-substrate linear-to-circular polarization metasurface converter," *IEEE Trans. Antennas Propag.*, vol. 68, no. 2, pp. 1186–1191, Feb. 2020.

[20] X. Gao, K. Li, X. Wu, C. Xue, G. Wang, X. Xie, and M. Qin, "Ultra-wideband linear-to-circular polarizer realized by bi-layer metasurfaces," *Opt. Exp.*, vol. 30, no. 11, pp. 18392–18401, 2022.

[21] A. K. Fahad, C. Ruan, R. Nazir, T. U. Haq, and W. He, "Dual-band ultrathin meta-array for polarization conversion in Ku/Ka-band with broadband transmission," *IEEE Antennas Wireless Propag. Lett.*, vol. 19, pp. 856–860, 2020.

[22] B.-Q. Lin, J. Guo, Y. Wang, Z. Wang, B. Huang, and X. Liu, "A wide-angle and wide-band circular polarizer using a bi-layer metasurface," *Prog. Electromagn. Res.*, vol. 161, pp. 125–133, 2018.

[23] H. Mirza, T. M. Hossain, P. J. Soh, M. F. Jamlos, M. N. Ramli, E. S. Hassan, A. A. Al-Hadi, and S. Yan, "Single layered swastika-shaped flexible linear-to-circular polarizer using textiles for S-band application," *Int. J. RF Microw. Comput.-Aided Eng.*, vol. 28, no. 7, Sep. 2018, Art. no. e21463.
[24] P. Fei, Z. Shen, X. Wen, and F. Nian, "A single-layer circular polarizer based on hybrid meander line and loop configuration," *IEEE Trans. Antennas Propag.*, vol. 63, no. 10, pp. 4609–4614, Oct. 2015.
[25] A. K. Fahad, R. Nazir, and C. Ruan, "Simple design of broadband polarizers using transmissive metasurfaces for dual band Ku/Ka band applications," *Sensors*, vol. 22, no. 23, p. 9152, Nov. 2022.
[26] Y. Li, J. Zhang, S. Qu, J. Wang, L. Zheng, Y. Pang, Z. Xu, and A. Zhang, "Achieving wide-band linear-to-circular polarization conversion using ultra-thin bi-layered metasurfaces," *J. Appl. Phys.*, vol. 117, no. 4, Jan. 2015, Art. no. 044501.
[27] B. Han, S. Li, X. Cao, J. Han, L. Jidi, and Y. Li, "Dual-band transmissive metasurface with linear to dual-circular polarization conversion simultaneously," *AIP Adv.*, vol. 10, no. 12, Dec. 2020, Art. no. 125025.
[28] M. A. Sofi, K. Saurav, and S. K. Koul, "Frequency-selective surface-based compact single substrate layer dual-band transmission-type linear-to-circular polarization converter," *IEEE Trans. Microw. Theory Techn.*, vol. 68, no. 10, pp. 4138–4149, Oct. 2020.
[29] O. Fernández, Á. Gómez, J. Basterrechea, and A. Vegas, "Reciprocal circular polarization handedness conversion using chiral metamaterials," *IEEE Antennas Wireless Propag. Lett.*, vol. 16, pp. 2307–2310, 2017.
[30] A. Majeed, J. Zhang, M. A. Ashraf, S. Memon, K. H. Mohammadani, M. Ishfaq, and M. Sun, "An ultra-wideband linear-to-circular polarization converter based on a circular, pie-shaped reflective metasurface," *Electronics*, vol. 11, no. 11, p. 1681, May 2022.
[31] Y. Jia, Y. Liu, W. Zhang, J. Wang, Y. Wang, S. Gong, and G. Liao, "Ultra-wideband metasurface with linear-to-circular polarization conversion of an electromagnetic wave," *Opt. Mater. Exp.*, vol. 8, no. 3, pp. 597–604, 2018.
[32] Y.-Z. Ran, L.-H. Shi, J.-B. Wang, S.-B. Wang, G.-M. Wang, and J.-G. Liang, "Ultra-wideband linear-to-circular polarization converter with ellipse-shaped metasurfaces," *Opt. Commun.*, vol. 451, pp. 124–128, Nov. 2019.
[33] B. Q. Lin, L. T. Lv, J. X. Guo, Z. L. Wang, S. Q. Huang, and Y. W. Wang, "Ultra-wideband linear-to-circular polarization conversion metasurface," *Chin. Phys. B*, vol. 29, no. 10, 2020, Art. no. 104205.
[34] M. Wang and Z. Zhai, "Wide-angle circular polarization converter based on a metasurface of Z-shaped unit cells," *Frontiers Phys.*, vol. 8, Oct. 2020, Art. no. 527394.
[35] S. X. Ta, I. Park, and R. W. Ziolkowski, "Crossed dipole antennas: A review," *IEEE Antennas Propag. Mag.*, vol. 57, no. 5, pp. 107–122, Oct. 2015.
[36] K. E. Kedze, H. Wang, Y. Kim, and I. Park, "Design of a reduced-size crossed-dipole antenna," *IEEE Trans. Antennas Propag.*, vol. 69, no. 2, pp. 689–697, Feb. 2021.

CHO HILARY SCOTT NKIMBENG received the B.Tech. degree in electrical and electronic engineering (telecommunication) from the University of Buea, Cameroon, in 2013, and the M.S. degree in electrical and computer engineering from Ajou University, Suwon, Republic of Korea, in 2018, where he is currently pursuing the Ph.D. degree with the Department of Electrical and Computer Engineering. His research interests include metasurface antennas, metamaterial-based antennas, circularly polarized antennas, miniaturized antennas, and bidirectional antennas.

HEESU WANG (Member, IEEE) received the B.S., M.S., and Ph.D. degrees in electrical and computer engineering from Ajou University, Suwon, Republic of Korea, in 2018, 2020, and 2024, respectively. He is currently a Postdoctoral Researcher with Ajou University. His research interests include the design of patch antennas, printed antennas, small antennas, and metasurface antennas for various wireless communication applications.

DAEYEONG YOON (Member, IEEE) received the B.S. degree in electrical and computer engineering and the integrated M.S./Ph.D. degree in AI convergence network from Ajou University, Suwon, South Korea, in 2018 and 2024, respectively. Since 2024, he has been a Postdoctoral Researcher with Ajou University. His research interests include periodic structures, frequency-selective surfaces, radomes, and radar cross sections.

YONG BAE PARK (Senior Member, IEEE) received the B.S., M.S., and Ph.D. degrees in electrical engineering from Korea Advanced Institute of Science and Technology, South Korea, in 1998, 2000, and 2003, respectively. From 2003 to 2006, he was with Korea Telecom Laboratory, Seoul, South Korea. He joined the School of Electrical and Computer Engineering, Ajou University, South Korea, in 2006, where he is currently a Professor. His research interests include electromagnetic field analysis, high-frequency methods, metamaterial antennas, radomes, and stealth technology.

HAEWOOK HAN received the B.S. and M.S. degrees in electrical engineering from Seoul National University, Seoul, Republic of Korea, in 1986 and 1988, respectively, and the Ph.D. degree in electrical engineering from the University of Illinois at Urbana-Champaign, USA, in 1995. From 1995 to 1997, he conducted semiconductor laser research with the AT&T Bell Laboratories, Murray Hill, NJ, USA. He is currently a Professor of electronic engineering with Pohang University of Science and Technology, Pohang, Republic of Korea. His current research interests include nano-bio terahertz photonics, compact terahertz sources (antennas and photomixers), high precision and real-time terahertz comb spectroscopy, terahertz photonic crystal fibers, terahertz biomedical sensing and imaging, terahertz near-field microscopy, terahertz hydration dynamics in biomolecular systems, and nanophotonic CMOS image sensors.

IKMO PARK (Member, IEEE) received the B.S. degree in electrical engineering from the State University of New York at Stony Brook and the M.S. and Ph.D. degrees in electrical engineering from the University of Illinois at Urbana-Champaign. He joined the Department of Electrical and Computer Engineering, Ajou University, Suwon, Republic of Korea, in 1996. He has authored and co-authored more than 400 technical journals and conference papers. He also holds more than 50 domestic and international patents. His present research interests include the design and analysis of microwave, millimeter-wave, terahertz wave, and nano-structured antennas with metamaterials and metasurfaces. He serves as chair, organizer, and member of program committees for various conferences, workshops, and short courses in electromagnetic-related topics. He was the Chair of the Department of Electrical and Computer Engineering, Ajou University, and a member of the Board of Directors of Korea Institute of Electromagnetic Engineering and Science (KIEES). He also serves as the Editor-in-Chief for *Journal of KIEES*, an Editorial Board Member for *International Journal of Antennas and Propagation* and *MDPI's Electronics*, and an Associate Editor for *IET's Electronics Letters*. He has also served as an Editorial Board Member of *Journal of Electromagnetic Engineering and Science*.